applied sciences

MDPI

Article

Region-Based Concave Point Matching for Separating Adhering Objects in Industrial X-Ray of Tungsten Ores

Rui Chen [1,*], Yan Zhang [2], Jie Cao [1], Yidong He [1] and Shumin Zhou [1]

[1] Jiangxi Province Engineering Research Center of New Energy Technology and Equipment, East China University of Technology, Nanchang 330013, China; 201561031@ecut.edu.cn (J.C.); heyidong@ecut.edu.cn (Y.H.); smzhou@ecut.edu.cn (S.Z.)
[2] National Key Laboratory of Uranium Resources Exploration-Mining and Nuclear Remote Sensing, East China University of Technology, Nanchang 330013, China; yanzhang@ecut.edu.cn
* Correspondence: chenrui@ecut.edu.cn

Abstract

Efficient and rational utilization of mineral resources significantly impacts economic and technological development. Image segmentation is a pivotal process in ore sorting, as its results directly affect the accuracy of mineral classification. Traditional segmentation methods often fail to meet the requirements for noise suppression, segmentation precision, and robustness in ore sorting. To address these issues, we propose an ore image segmentation method based on concavity matching via region retrieval, which comprises a contour approximation module, a concavity matching module, and a segmentation detection module. It introduces the concepts of single-contour, multi-contour, and segmentation regions in ore images, offering tailored segmentation approaches for varying adhesion forms and quantities. A significant contribution of this study lies in the contour approximation module, which simplifies the edge information of ore images via curve fitting, effectively removing the influence of edge noise points. The concavity matching module restricts candidate areas for matching concavity points through the construction of search regions, significantly improving matching accuracy. Finally, paired concavity points are connected to completing the segmentation process. Experimental comparisons using X-ray images of tungsten ores demonstrate that the proposed method can effectively suppress noise-induced concavity interference, achieving a noise reduction efficiency of 94.77% and a concavity region search accuracy of 93.60%, thus meeting the precision requirements for segmenting X-ray ore images. Given its high efficiency and accuracy, industrial sectors involved in mineral processing are recommended to incorporate this segmentation method into intelligent ore sorting equipment upgrading and renovation projects, enhancing the overall efficiency of mineral resource sorting and promoting the sustainable development of the mineral industry.

Keywords: ore image segmentation; dual-energy X-ray; concavity matching; contour approximation; region retrieval

check for updates

Academic Editor: Seokwon Yeom

Received: 28 July 2025
Revised: 24 August 2025
Accepted: 27 August 2025
Published: 4 September 2025

Citation: Chen, R.; Zhang, Y.; Cao, J.; He, Y.; Zhou, S. Region-Based Concave Point Matching for Separating Adhering Objects in Industrial X-Ray of Tungsten Ores. *Appl. Sci.* **2025**, *15*, 9712. https://doi.org/10.3390/app15179712

Copyright: © 2025 by the authors. Licensee MDPI, Basel, Switzerland. This article is an open access article distributed under the terms and conditions of the Creative Commons Attribution (CC BY) license (https://creativecommons.org/licenses/by/4.0/).

1. Introduction

In recent years, machine vision has found extensive applications in the field of mineral separation [1,2]. In industrial settings, ore sorting devices based on X-ray transmission imaging technology are commonly employed for mineral classification [3,4]. The sorting process is illustrated in Figure 1. During the imaging of crushed ore particles on conveyor belts, particle adhesion and overlap often occur. That will lead to multiple distinct ore

particles being identified as a single target during content recognition and localization, resulting in misclassification of mineral types and erroneous coordinate registration. These issues further cause ineffective ejection, lower sorting efficiency, and reduced target mineral content in the sorted products. Therefore, prior to determining the coordinates, it is crucial to segment overlapping and adhered ore images into individual particles and ensure accurate classification and coordinate registration for each particle [5–9].

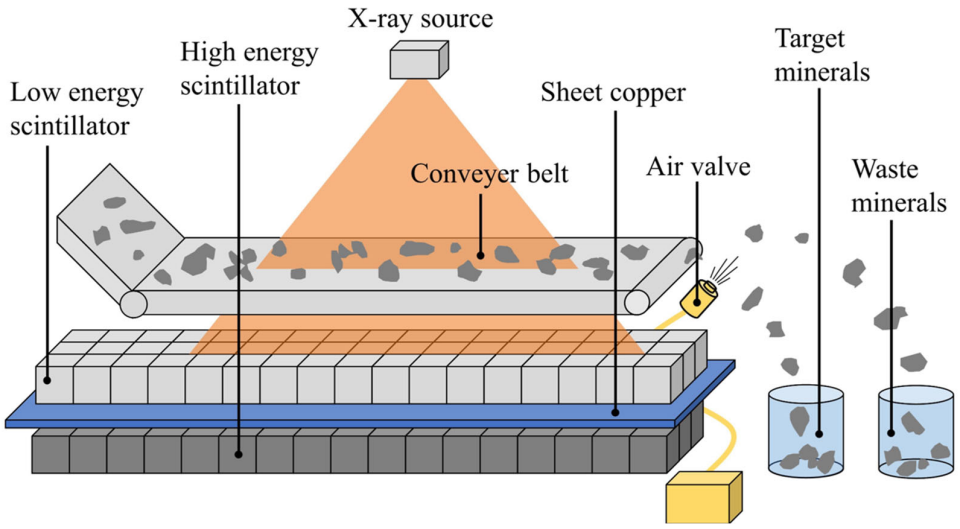

Figure 1. Dual-energy X-ray mineral sorting process.

Currently, segmentation algorithms for processing adhered and overlapping ore images are typically based on methods such as thresholding, edge detection, region analysis, clustering, morphology, concavity detection, and deep learning [10–14]. Among these, concavity detection and matching algorithms are widely used for segmenting adhered images due to their simplicity and clarity of steps, achieving significant results [15–18], but existing approaches have critical limitations that hinder industrial applicability to tungsten ore X-ray images:

(I) Noise-induced false concave points and over-segmentation: WANG et al. [19] identified concave points via three-point angle calculation, but this method is computationally intensive and fails to filter false concave points caused by irregular, rough ore edges (a common feature of crushed tungsten ores). HE et al. [20] improved concave point detection with directional constraints, but the core principle still generates excessive noise points, leading to severe over-segmentation that misidentifies ore surface texture as adhesion boundaries.

(II) Poor adaptability to multi-contour and complex adhesion: SUN et al. [21] relied on concave region identification, but it fails when adhesion-induced concavities are indistinct. Most traditional methods only address single-contour adhesion (2–3 particles) and cannot handle multi-contour scenarios (e.g., inner contours formed by 4+ adhering particles, which account for 12.21% of industrial tungsten ore samples, Table 1) or complex adhesion forms.

Table 1. The adhesion form and quantity distribution of ores.

Adhesive Form	Single-Contour				Multi-Contour	Totality
	2 Adhesion	3 Adhesion	4 Adhesion	>4 Adhesion		
Quantity	208	112	73	63	60	516
proportion	40.31%	21.71%	14.15%	12.21%	11.63%	

Based on the aforementioned limitations of existing studies, two critical research gaps persist in the current literature on ore image segmentation. First, no concavity matching method has been developed to simultaneously address edge noise suppression (to eliminate false concave points induced by the rough, irregular edges of crushed tungsten ores) and adaptability to both single-contour and multi-contour adhesion forms—leaving complex scenarios (such as multi-contour adhesion or adhesion of 4 or more tungsten ore particles, which account for a non-negligible proportion of industrial samples) unaddressed and failing to meet the diverse needs of real-world tungsten ore sorting. Second, there is a lack of effective validation mechanisms to verify whether segmentation results align with the actual physical structure of ores; existing methods only evaluate algorithm performance based on image-level metrics (e.g., concave point detection rate) rather than linking outputs to the physical properties of ores (e.g., density-based grayscale distribution in X-ray images). This disconnect between algorithmic results and industrial sorting requirements often leads to "theoretically valid but practically invalid" segmentation, directly compromising the accuracy of ore sorting and mineral recovery efficiency.

To address these challenges, we propose a concave point detection and matching algorithm for adhered and overlapping ore images based on polygon fitting. First, ore images are preprocessed to generate polygonal representations. Next, search regions are constructed based on polygon vertices, where candidate points for concave matching are detected. Finally, a detection line array is introduced to assess segmentation regions, ensuring enhanced segmentation accuracy. Experimental results demonstrate that the proposed algorithm effectively suppresses noise concave points and achieves high segmentation precision and operational efficiency.

The remaining structure of this study is organized as follows: Section 2 elaborates on the technical details of contour approximation and concave point identification, including the polygon fitting process for edge smoothing and the circular region-based method for distinguishing concave from convex vertices. Section 3 presents the core concave point matching method: it first details the directional search region construction and matching logic for single-contour adhered images, then extends the approach to multi-contour scenarios (focusing on inner contour concave point matching), and finally introduces the grayscale standard deviation-based segmentation validation mechanism. Section 4 reports the experimental design and results, including the tungsten ore dataset (source, particle size, and adhesion form distribution), test equipment parameters, and comparative analyses of the proposed method's denoising efficiency, segmentation accuracy, runtime, and sorting performance against four traditional algorithms. Section 5 concludes with a summary of key findings, discusses the method's industrial implications, and highlights future research directions.

2. Preprocessing and Concave Point Detection

The X-ray transmission image of tungsten ore is shown in Figure 2a, and its corresponding binary image is presented in Figure 2b. In subsequent steps, the contour information of the binary image is extracted, and the contour coordinates are sequentially output. These data are used to determine the adhesion forms within ore piles, facilitating the application of appropriate processing methods for efficient handling. Due to the irregular shape and size of ore particles, concave pits of varying dimensions along the edges can significantly interfere with concave point detection, often leading to over-segmentation. To eliminate most noise-induced concave points, a polygon fitting algorithm is introduced to approximate the binary image of the ore as a polygonal representation for further processing [22]. Figure 2c shows the inner contour edge of an adhered ore image, which, after polygon

fitting, results in the polygonal image illustrated in Figure 2d. This fitting process smooths the rough edges of the ore image and eliminates small concave pits along the edges.

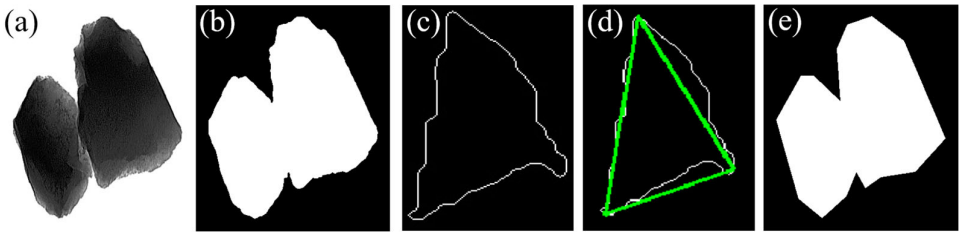

Figure 2. Image preprocessing and polygon fitting. (**a**) image of tungsten ore. (**b**) corresponding binary image. (**c**) inner contour edge of adhered ore image. (**d**) polygonal process. (**e**) smooth the rough edges of the ore image.

Simplified edge information reduces computational complexity, optimizing subsequent image processing steps. The polygon fitting procedure is as follows:

(I) Contour Extraction: The Suzuki method is employed to extract the contour information from the foreground region of the binary image [23].

(II) Polygon Vertex Extraction: The coordinates of the polygon vertices are derived from the contour information, and all vertex coordinates are sequentially connected.

(III) Polygon Image Construction: The internal area of the polygon is filled with white to generate the polygonal binary image, as shown in Figure 2e.

The degree of fitting determines the number of vertices in the resulting polygonal image, affecting the level of detail retained. By using polygonal images as the input for segmentation algorithms, interference from most noise points is effectively suppressed, which significantly enhances the accuracy of concave point detection and mitigates the risk of over-segmentation.

Figure 3a highlights all vertices in the polygonal ore image, including concave points. Circular regions are constructed with these vertices as their centers, ensuring that each region contains both foreground pixels (white) and background pixels (black), as illustrated in Figure 3b,c. The proportion of foreground pixels within a circular region serves as an indicator of the concavity of the corresponding vertex. Specifically, circular regions centered on concave points are expected to have a foreground pixel ratio exceeding 50%, whereas those centered on non-concave points exhibit a ratio of 50% or less. As depicted in Figure 3b, the foreground pixel ratio in the circular region exceeds 50%, confirming the vertex as a concave point.

In contrast, the circular region shown in Figure 3c has a foreground pixel ratio below 50% (<180°), identifying the vertex as convex. To reduce the impact of noisy concave points that may cause over-segmentation, threshold far greater than 50% (70% is employed). By systematically examining all vertices, the method successfully identifies all concave points in the binary polygonal image, as shown in Figure 3d.

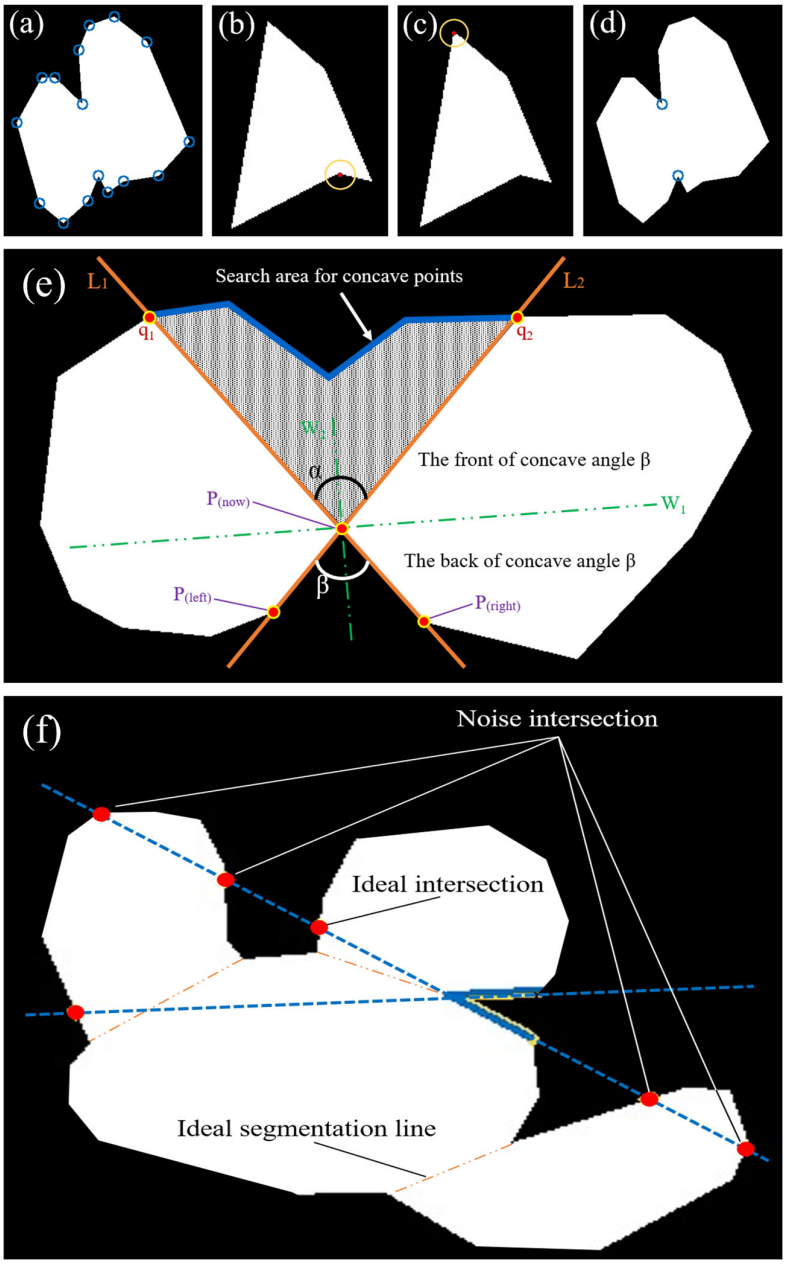

Figure 3. The process of identifying concave points. (**a**) all vertices in the polygonal ore image. (**b**) concave points identification. (**c**) non-concave points identification. (**d**) all concave points identification. (**e**) The process of concave point matching (region retrieval). (**f**) Complex adhesive forms form multiple interference intersections.

3. Concave Point Matching Method

The choice of concave points matching as the core segmentation strategy is rooted in two key considerations: morphological adaptability to ore adhesion and circumvention of traditional method limitations.

Industrial tungsten ore particles, after crushing and transportation, form adhesion structures where the contact boundary between adjacent particles inherently presents a concave contour (Figure 2). This concave feature is a "bite-type" contact trace formed by the natural stacking of independent ore contours, serving as a direct visual marker to distinguish "adhered regions" from "independent particles." Unlike indirect features such as grayscale differences (relied on by thresholding methods) or contour changes (used in edge detection), concave points, as intrinsic attributes of adhesion regions, enable more

accurate localization of segmentation boundaries, ensuring consistency between results and the actual ore morphology.

Compared with existing techniques, the proposed concave point matching method achieves breakthroughs in noise suppression, scenario adaptability, and segmentation robustness through modular innovations.

3.1. Concave Point Matching Method for Single-Contour Images

If the preprocessed adhered ore image contains only a single contour, this case is defined as a single contour adhered image, as shown in Figure 2b. In the polygonal binary image, any concave point can be selected as the current concave point $P_{now}(x_1, y_1)$, since the coordinates of the inflection points in the polygonal image are stored sequentially, the coordinates of the inflection points on both sides of P_{now}, denoted as $\mathrm{P_{left}}\ (\mathrm{x_0}, \mathrm{y_0})$ and $P_{right}(x_2, y_2)$, can be directly retrieved. As illustrated in Figure 3e, two lines that intersect at P_{now} can be constructed using P_{now} and its adjacent inflection points, denoted as $\mathrm{L_1}$ and $\mathrm{L_2}$. The general equation of these lines is expressed as:

$$\begin{cases} A_1 x + B_1 y + C_1 = 0 \\ A_2 x + B_2 y + C_2 = 0 \end{cases} \tag{1}$$

The coefficients of the equation can be determined based on the given coordinates as follows:

$$\begin{cases} A_1 = y_1 - y_0 & B_1 = x_0 - x_1 & C_1 = x_1 y_0 - x_0 y_1 \\ A_2 = y_1 - y_2 & B_2 = x_2 - x_1 & C_2 = x_1 y_2 - x_2 y_1 \end{cases} \tag{2}$$

At point $\mathrm{P_{now}}$, the lines $\mathrm{L_1}$ and $\mathrm{L_2}$ form an angle α, where the sides of α define the detection range of the concave point, as illustrated by the shaded area in Figure 3e. The contour within this detection range is identified as the target contour segment, shown as the blue line segment in Figure 3e. By using the intersections $\mathrm{q_1}, \mathrm{q_2}$ of the lines $\mathrm{L_1}, \mathrm{L_2}$ with the image contour as the start and end coordinates, all coordinate sequences of the target contour segment can be retrieved from the contour coordinates. Within this sequence, the connection point for P_{now} is sought to complete the concave point matching. However, aside from q_1 and q_2, other points on segments $P_{now}P_{left}$ and $P_{now}P_{right}$ may also serve as intersections of L_1, L_2 with the image contour, significantly interfering with the selection of q_1, q_2, thereby causing errors in locating the target contour segment. Angular bisectors are employed to filter out interfering intersections to address the issue above. The slope of the angular bisectors can be derived based on the slopes of L_1, L_2, using the following Equation:

$$k^2 + \frac{2(1 - k_1 k_2)}{k_1 + k_2} k - 1 = 0 \tag{3}$$

here, k_1, k_2 represents the slope of the line L_1 and L_2, respectively. The above equation has two roots, which correspond to the slopes of the two angular bisectors, k_3 and k_4. These angular bisectors are denoted as w_1 and w_2. Since the slopes of the two angular bisectors are known and both pass through P_{now}, their point-slope equations can be expressed as:

$$w_1 : y - y_1 = k_3(x - x_1) \qquad w_2 : y - y_1 = k_4(x - x_1) \tag{4}$$

by transforming these equations, the general form of the angular bisector w_1, w_2 can be expressed as:

$$\begin{cases} A_3 = k_3 & B_3 = -1 & C_3 = y_1 - k_3 x_1 \\ A_4 = k_4 & B_4 = -1 & C_4 = y_1 - k_4 x_1 \end{cases} \quad (5)$$

The positions of points P_{left} and P_{right} relative to the angular bisectors can be used to distinguish between the two bisectors. If both P_{left} and P_{right} are located on the same side of one bisector, it is labeled as w_1; otherwise, it is labeled as w_2. The bisector w_1 separates the segments $P_{now}P_{left}$, $P_{now}P_{right}$, and the target contour segment, serving as a tool for identifying and eliminating noise intersections. The segment $P_{now}P_{left}$ and $P_{now}P_{right}$ form a concave angle β at point P_{now}, as shown in Figure 3e. Using the angular bisector w_1 as a reference line, the side containing P_{left} and P_{right} is defined as the "back" of β, while the opposite side is the "front", all intersections located on the back side of β need to be filtered out, as they are noise intersections on segments $P_{now}P_{left}$ and $P_{now}P_{right}$.

Through the operations described above, the intersection points q_1 and q_2 on the target contour segment can be accurately identified. However, during the processing, certain ore images may present multiple interfering intersection points, as illustrated in Figure 3f. Due to the presence of the angular bisector w_1, noise intersections on the "back" side of β can be easily identified and filtered out and the noise intersections on the "front" side of β can be eliminated by evaluating their distance from point P_{now}, only the intersection point closest to P_{now} is retained. Once the precise intersection points q_1 and q_2 are obtained, they divide the image contour into two segments. The segment that does not include P_{now} is designated as the target contour segment. By iterating through all coordinates in the target contour segment:

(I) If there is exactly one concave point within the target contour segment, that point is selected as the candidate connection point for P_{now};
(II) If multiple concave points exist, the one closest to P_{now} is selected as the candidate connection point.
(III) If no concave points are present, any point in the target contour segment that is closest to P_{now} is chosen as the candidate connection point. In this case, the candidate connection point does not need to be a concave point.

After completing the matching process for the current concave point P_{now}, P_{now} is replaced by another concave point on the image contour, and the process is repeated to identify its candidate connection point. If a concave point has already been selected as the candidate connection point for another concave point, it does not require further matching, and then, P_{now} is replaced by the next concave point. This process continues until all concave points are either processed or designated as candidate connection points, at which point the concave point matching phase is complete.

3.2. Concave Point Matching Method for Multi-Contour Images

After extracting the contour information from the ore image, the number of contours and the distinction between inner and outer contours can be easily identified. If the adhered ore image contains at least two contours, it is defined as a multi-contour adhesion, as shown in Figure 4a. The corresponding binary image is presented in Figure 4b, and the polygonal representation is shown in Figure 4c. For multi-contour images, only the concave points on the inner contours require matching, while the concave points on the outer contours do not undergo this process. Figure 4d,e mark the concave points on the outer and inner contours, respectively, of a multi-contour adhered image. Figure 4f–i demonstrate the matching process for each concave point on the inner contour, the algorithm iterates through all

concave points on the inner contour, searching for candidate connection points within the corresponding detection regions. The segmentation result is shown in Figure 4j.

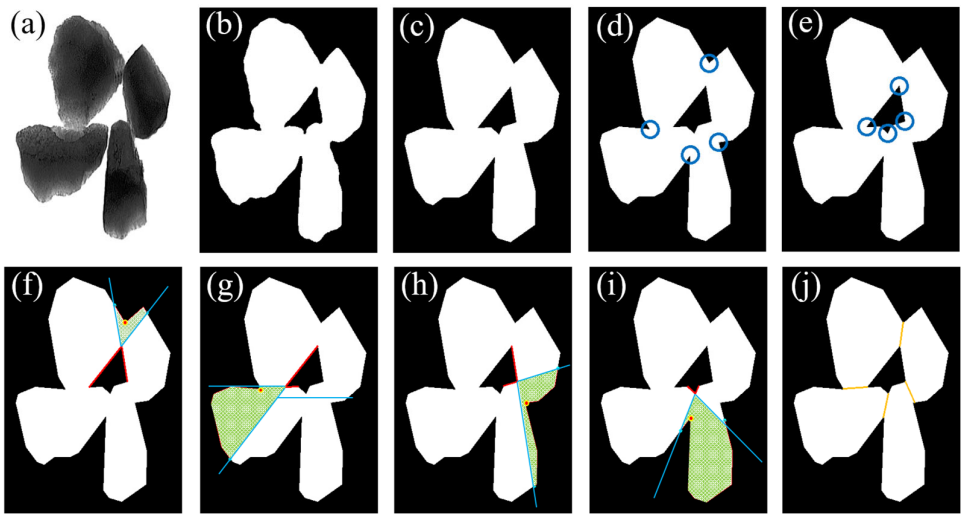

Figure 4. Concave point matching process and segmentation results of multi contour images (**a**) multi-contour adhesion. (**b**) corresponding binary image. (**c**) polygonal representation. (**d**) concave points outer contours. (**e**) concave points inner contours. (**f**–**i**) matching process for each concave point on the inner contour. (**j**) segmentation result.

3.3. Segmentation Validation

Once concave point matching is completed, the paired concave points are connected to form segmentation lines. To improve the segmentation accuracy, we further validate the segmentation results. The concave point detection and matching processes are based on the binary image, which introduces a certain level of ambiguity. In contrast, grayscale images provide a more accurate representation of the ore's actual shape and the adhesion forms between ores, making it easier to determine whether the segmentation is correct. The position of the segmentation line is defined as the region to be segmented. To avoid over-segmentation, we construct a detection line array within the target segmentation region of the grayscale image, using the segmentation line as a reference; this step further verifies segmentation accuracy. Each segmentation line generates a corresponding detection line array, which consists of three-line segments perpendicular to the segmentation line, as illustrated in Figure 5a.

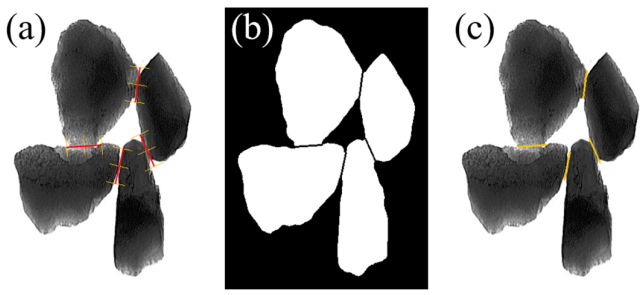

Figure 5. Segmentation detection line array and segmentation effect. (**a**) three-line segments perpendicular to the segmentation line. (**b**) segmented binary image. (**c**) segmentation line on the grayscale image of ore.

During the detection process, the Bresenham line algorithm is used to obtain the pixel coordinates of the detection line array and extract the grayscale values at those coordinates [24]. The standard deviation σ of the grayscale values collected along each

detection line is then calculated. Figure 6 illustrates the standard deviation of detection lines at various positions in the ore image. Detection lines located at adhesion regions exhibit more significant variations in pixel grayscale values, resulting in higher standard deviations. Conversely, detection lines on the ore body show more minor variations in pixel grayscale values, leading to lower standard deviations. For a detection line array, if at least one standard deviation exceeds a predefined threshold, it indicates that the detection line intersects the adhesion area between ores, confirming the correctness of the segmentation. Otherwise, the current segmentation line is located within a single ore body, and the segmentation process should be terminated. If segmentation validation is successful, the segmentation result is retained, yielding a segmented binary image as shown in Figure 5b. The segmentation line is then overlaid on the grayscale image of the ore, as shown in Figure 5c, and segmentation flowchart of adhesive ore images is shown in Figure 7.

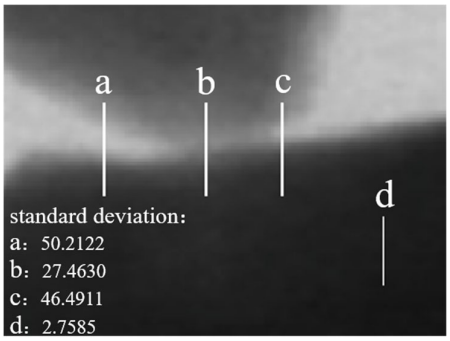

Figure 6. Distribution of detection lines and comparison of standard deviations.

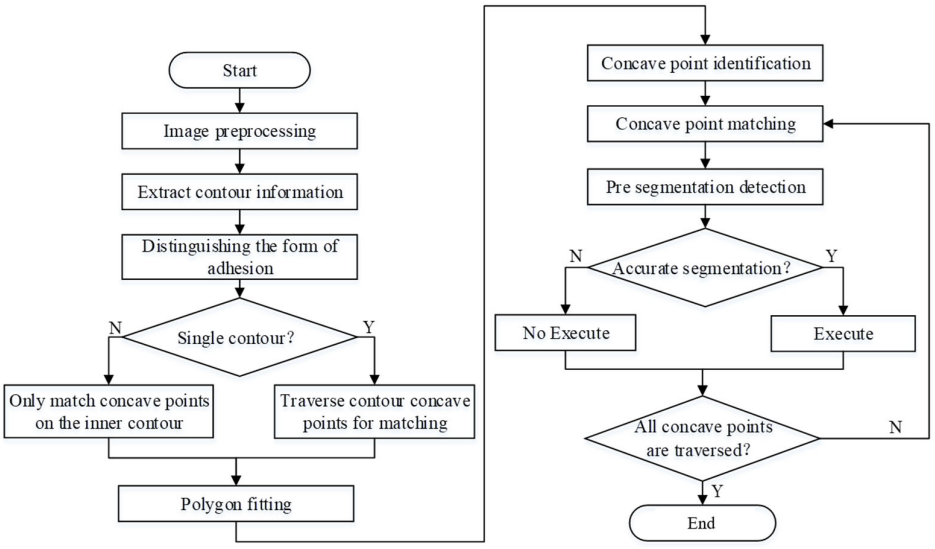

Figure 7. Segmentation flowchart of adhesive ore images.

3.4. Analysis of Algorithm Advantages

For any given concave point, its connection point should ideally also be a concave point. Therefore, the algorithm prioritizes pairing P_{now} with concave points within the target contour segment. However, during polygonal fitting, actual concave points with subtle depressions are often smoothed out, resulting in the absence of concave points within P_{now}'s search area. To address the issue above, the algorithm selects, within the defined range, the point closest to P_{now} as its connection point, ensuring that every concave point can be linked. In addition, noisy concave points with significant depressions near the edges

of ore images are unlikely to be smoothed during polygonal fitting and may be mistakenly treated as actual concave points during matching. To mitigate the impact of such noise on the segmentation results, the algorithm constrains the detection direction and area for selecting connection points by constructing two lines at P_{now}, which ensures that concave points outside the target contour segment are excluded, and P_{now}'s connection point is chosen solely within a specific region. This mechanism ensures that the segmentation results align closely with actual conditions. It is also possible that the detection angle and region for concave points are set too narrowly during segmentation. In exceptional cases, as shown in Figure 8, overly restricted detection ranges may prevent actual concave points from being correctly matched; however, the algorithm can still select a connection point close to the actual concave point based on the minimum distance principle, keeping the segmentation results within an acceptable error range.

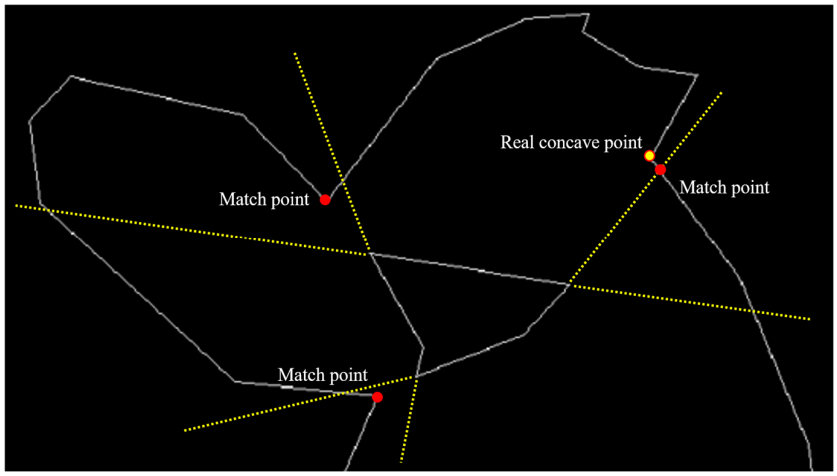

Figure 8. Special situations that may occur during the concave point matching process.

In summary, after identifying the target contour segment, P_{now} will always be paired with a unique, high-quality connection point. This mechanism compensates for the loss of actual concave points due to smoothing caused by subtle depressions while avoiding unreasonable matches. As a result, the segmentation outcomes are more consistent with actual conditions.

4. Experimental Results and Discussion

4.1. Experimental Data and Equipment

The tungsten ore samples used in this study come from the mine in Baipi Township, Chongren County, Jiangxi Province, China. The tungsten ore used for imaging in the test process has a particle size distribution of about 50–95 mm and a thickness distribution of about 10–45 mm. The ore samples are shown in Figure 9a, and a custom dataset of 516 tungsten ore adhesion images was created for image segmentation experiments, with the distribution of adhesion forms and quantities summarized in Table 1. The test platform is the HPY SORTING X1400 Intelligent Ore Sorting Machine (Ganzhou, China) is shown in Figure 9b, with the following equipment parameters:

(I) Volume: 9500 mm × 1900 mm × 2100 mm;
(II) Weight: 10 tones;
(III) Overall machine power 15 KW;
(IV) Sorting particle size 40 mm–100 mm;
(V) Processing capacity of 60–100 (T/h).

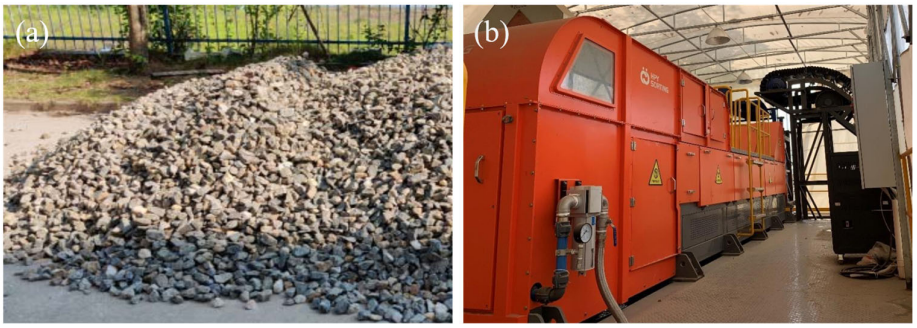

Figure 9. (**a**) Tungsten ore samples. (**b**) XRT intelligent ore sorting machine.

In the experiment, the image processing equipment (HPY SORTING X1400, Ganzhou, China) has 8GB of memory, the CPU model is AMD Ryzen 5 2500U 2.00GHz, windows 10 operating system, and the algorithm is implemented by OpenCV library.

4.2. The Segmentation Effect of Images

Various segmentation algorithms exhibit different levels of suitability for different datasets. Methods based on thresholding, edge detection, region-based approaches, clustering, morphological operations, and deep learning generally perform well in specific segmentation scenarios. However, due to the unique physical shapes of ores and the highly intricate adhesion patterns between them, these conventional methods lack specificity for mineral images and deliver suboptimal segmentation results. To address this, the improved concave point detection and matching algorithm proposed in this paper was compared against other methods, including the contour line method [16], the concavity defect method [17], the linear method [18], and the conjugate line method [19]. The segmentation results of these methods are shown in Figure 10. Column (a) presents the original ore images, while columns (b), (c), (d), and (e) display the results of concave point detection and segmentation using the contour line method, concavity defect method, linear method, and conjugate line method, respectively. Column (f) shows the results of the proposed algorithm.

The proposed algorithm simplifies the image through polygonal fitting, effectively filtering out noisy concave points and avoiding over-segmentation. Furthermore, it enforces concave point matching by searching for connection points within specific regions, thereby preventing under-segmentation. Lastly, a detection line array is constructed to evaluate the grayscale values of the segmented regions, ensuring accurate segmentation. Unlike other methods, the proposed approach is not constrained by the number or type of ore adhesions and demonstrates significantly superior segmentation performance.

4.3. Denoising Rate of Concave Points

Concave point detection is a critical step in the segmentation process, as its accuracy directly impacts the segmentation results. Increasing the resolution of ore images tends to exacerbate edge roughness and introduce more noisy concave points, negatively affecting the quality of detection. To more intuitively evaluate the denoising capability of the algorithm, 100 ore image samples were randomly selected and processed into versions with varying resolutions. These versions were then tested for their ability to suppress noisy concave points, with the denoising performance quantitatively assessed using the noisy concave point rate R_{noise}, defined as:

$$R_{noise} = \frac{N_{pit(detect)} - N_{pit(correct)}}{N_{pit(detect)}} \quad (6)$$

where $N_{pit(detect)}$ represents the total number of detected concave points in an image at a specific resolution, and $N_{pit(correct)}$ denotes the number of true concave points. The average noisy concave point rate ($\overline{R_noise}$) for each method across different resolutions was calculated as:

$$\overline{R_{noise}} = \frac{\sum_{i=1}^{n} R_{noise_i}}{n} \quad (7)$$

where n = 100, representing the number of samples. The denoising efficiency of each method was then computed based on $\overline{R_{noise}}$, as shown in Figure 11. The proposed algorithm achieved a concave point denoising efficiency as high as 94.77%, indicating that the polygonal fitting operation effectively smooths the rough edges of ore images. Which significantly suppresses noise-induced concave points caused by resolution changes or edge roughness, underscoring the algorithm's strong denoising capability and providing a solid foundation for accurate concave point detection.

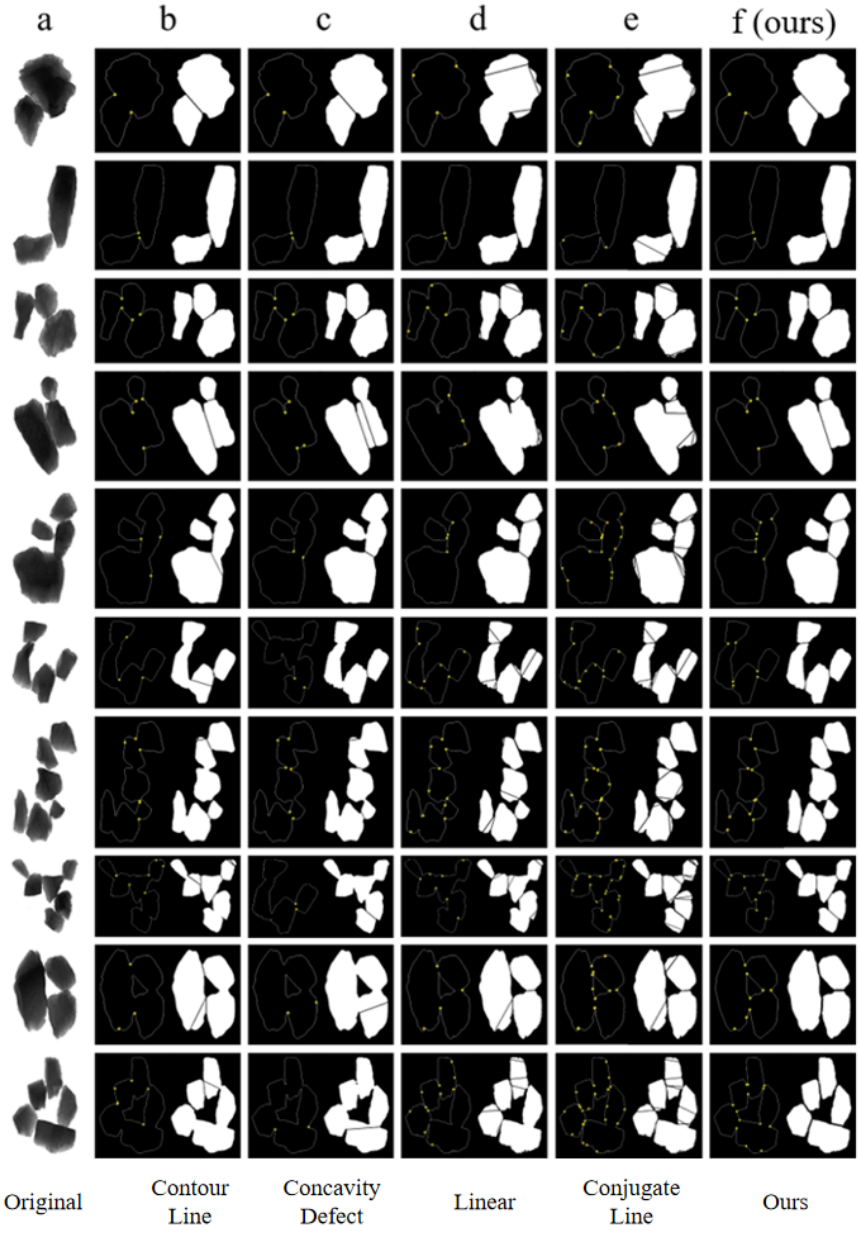

Figure 10. The concave point detection effect and final segmentation effect of various algorithms (**a**) original ore images. (**b**) contour line method. (**c**) concavity defect method. (**d**) linear method. (**e**) conjugate line method. (**f**) our method.

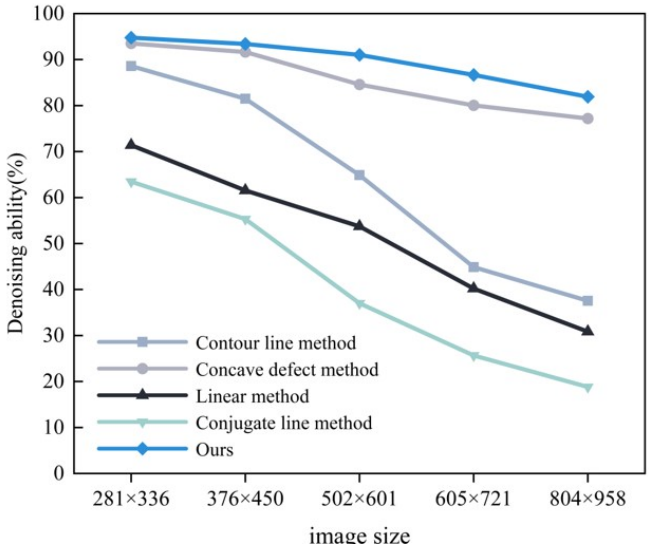

Figure 11. Comparison of denoising performance of concave points.

4.4. Accuracy of Segmentation

Segmentation accuracy is used to compare the overall segmentation performance of different algorithms. Various algorithms were employed to segment the images, and the segmentation results were categorized into precise segmentation, incorrect segmentation, over-segmentation, under-segmentation, and effective segmentation. The quantities for each category are recorded in Figure 12.

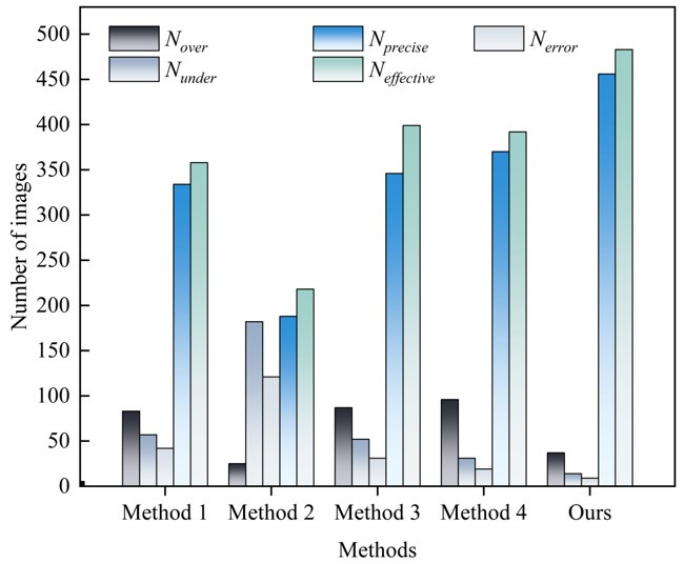

Figure 12. Classification and statistical results of segmentation effects.

$N_{precise}$: The number of precisely segmented images. These images are segmented entirely according to the actual distribution of the ore.

N_{error}: The number of incorrectly segmented images. These images exhibit no correct segmentation at the actual adhesion areas, showing only erroneous or missing segmentation.

N_{over}: The number of over-segmented images. In addition to correct segmentation at actual adhesion areas, these images also exhibit erroneous segmentations.

N_{under}: The number of under-segmented images. These images fail to segment certain actual adhesion areas.

The above categories encompass all segmentation results. The number of effectively segmented images ($N_{effective}$) includes precisely segmented images as well as those from

other categories with segmentation errors that do not affect the positioning of the blast center during the sorting process. The overall segmentation accuracy ($AC_{segment}$) is used to measure the comprehensive segmentation performance of different algorithms, and the data is summarized in Table 2. The formula for $AC_{segment}$ is defined as:

$$AC_{segment} = \frac{N_{effective}}{N_{precise} + N_{error} + N_{over} + N_{under}} \times 100\% \quad (8)$$

Table 2. Overall segmentation accuracy of each algorithm.

Method	$AC_{segment}$ (%)
Contour line method	69.38
Concave defect method	42.25
Linear method	77.33
Conjugate line method	75.97
Ours	93.60

The data in Figure 12 and Table 2 show that the proposed algorithm achieves the highest number of effectively segmented images compared to other methods. It produces the fewest over-segmented, under-segmented, and incorrectly segmented images when processing the same dataset and achieves the highest overall segmentation accuracy.

In adhered ore images, those with two adhered targets are the easiest to segment, and existing algorithms generally perform well for ore images with two adhered targets. However, as the number of adhered targets increases and adhesion patterns become more complex, the segmentation performance of these algorithms inevitably declines. To further improve the effective segmentation rate, an algorithm must be capable of handling multi-target and multi-contour adhered ore images. Figure 13 illustrates the effective segmentation rates of different algorithms for ore images with varying numbers of adhered targets and different adhesion patterns. Compared to other algorithms, the proposed method consistently achieves higher effective segmentation rates across scenarios involving two targets, three targets, four targets, and more than four targets, as well as multi-contour adhesion. Moreover, its performance remains relatively stable, demonstrating a more robust capability to handle complex adhered ore images.

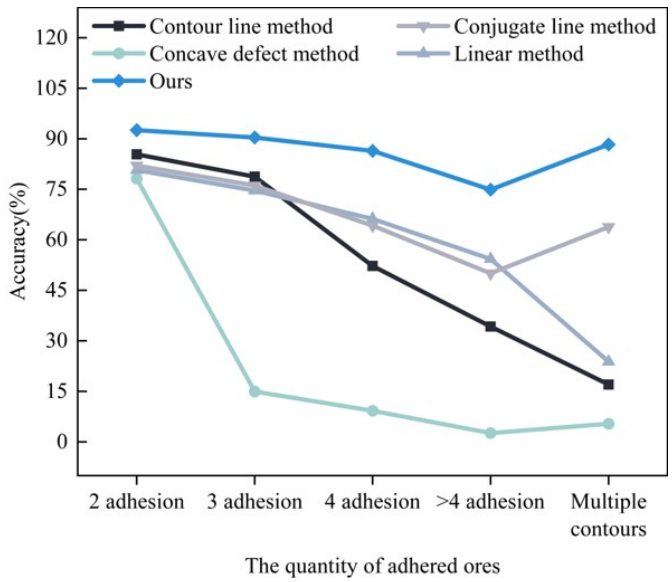

Figure 13. Effective segmentation rates of various algorithms for images with different adhesive forms.

4.5. Algorithm Running Efficiency and Sorting Efficiency

Figure 14 presents the average computation time required by different algorithms to process 100 adhered ore images at various resolution levels. It is evident that the proposed algorithm achieves the shortest computation time across all image specifications, with highly stable runtime performance. For instance, the algorithm processes images with dimensions of 281 × 336 in an average time of just 5.13 ms, and the detection efficiency can be improved by more than 220 times.

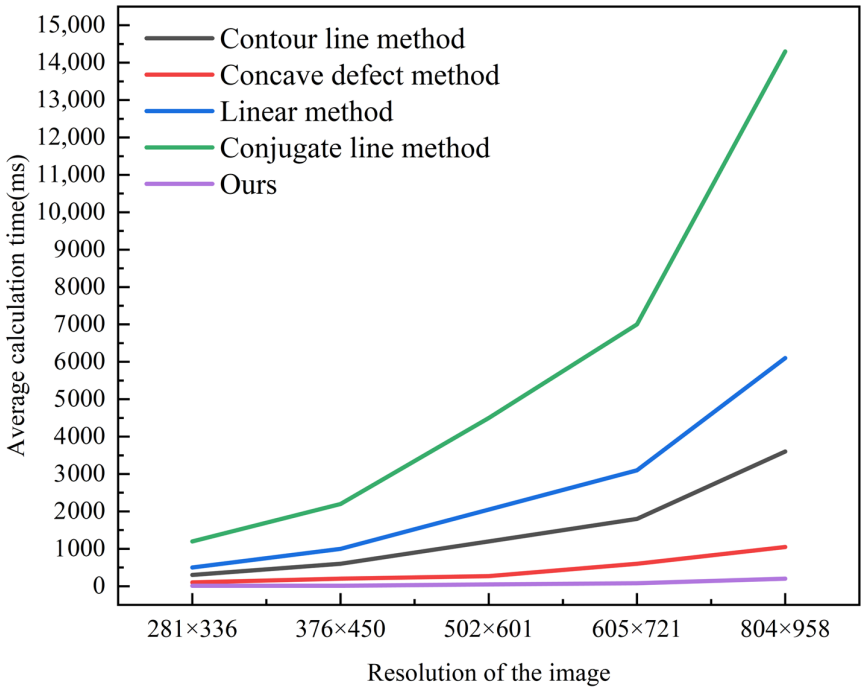

Figure 14. The average computation time of each algorithm.

To evaluate the performance of different segmentation algorithms in mineral separation, tungsten ore samples with an impurity content and a size range of 55–90 mm were selected for testing. During the mineral separation process, various segmentation algorithms were applied to the adhered ore images. The WO_3 content in the separated tungsten ore serves as an indicator of the effectiveness of these algorithms in enhancing mineral separation performance. The tungsten ore sample with a WO_3 content of 5.21% was separated using beneficiation equipment, during which different segmentation algorithms were applied to the tungsten ore images for segmentation processing. Table 3 records the WO_3 content of the mineral in the sample after direct separation by the beneficiation equipment, as well as the WO_3 content of the mineral after separation by the equipment under the influence of different segmentation algorithms. From the data, integrating segmentation algorithms helps increase the content of the target mineral in the separation product, thereby optimizing the separation efficiency. Compared to other segmentation methods, the proposed algorithm shows outstanding performance in enhancing separation efficiency, achieving a maximum increase of 34.46% in tungsten content in the final product.

Table 3. WO_3 content of minerals processed by different segmentation methods.

Image Processing Methods	Tungsten Content (%)
Not processing	26.67
Contour line method	39.81
Concave defect method	31.60

Table 3. *Cont.*

Image Processing Methods	Tungsten Content (%)
Linear method	48.79
Conjugate line method	47.32
Ours	61.13

5. Discussion and Conclusions

The core value of the X-ray image segmentation algorithm for tungsten ore proposed in this study lies in addressing three critical challenges in X-ray image segmentation of industrial tungsten ores: noise suppression, adaptation to complex adhesion scenarios, and verification of result authenticity:

(1) Through the contour approximation module based on polygon fitting, a concave point denoising efficiency of 94.77% was achieved (Section 4.3), significantly outperforming the traditional contour line method and concavity defect method. This breakthrough fills the technical gap in "filtering false concave points in ores with rough edges (e.g., crushed tungsten ores)". The proposed algorithm, through a dual mechanism of "fitting smoothing + circular region verification", reduces noise interference to less than 5%, providing a new paradigm for accurate segmentation of high-noise mineral images.

(2) A scenario-specific matching strategy was developed for single-contour (2–4 particles) and multi-contour (>4 particles) adhesion scenarios, achieving an effective segmentation rate of 92.3% for multi-contour adhered images (Section 4.4)—a 16.3-percentage-point improvement over the conjugate line method. This design directly addresses an industrial pain point: Table 1 shows that multi-contour and >4-particle adhesion samples account for 23.84% of the total, and traditional methods lack the capability to handle such scenarios. The adaptability of the proposed algorithm enables it to cover over 85% of adhesion morphologies of industrial tungsten ores, laying a foundation for the application of large-scale sorting equipment.

(3) An innovative grayscale standard deviation verification module was introduced. By leveraging the physical correlation between ore density and X-ray grayscale ($\sigma > 6$ for adhesion regions, $\sigma < 5$ for single ores), the "physical authenticity" of segmentation results was incorporated into the evaluation system. This avoids the defect of traditional algorithms—"image-level correctness but industrial-level ineffectiveness".

The technical achievements of this study essentially respond to the urgent global demand for efficient utilization of mineral resources. In recent years, the strategic value of mineral resources and the supply-demand imbalance have become core topics in the economic field. The proposed algorithm can increase the target mineral recovery rate of tungsten ore sorting to over 88%. As shown in Table 3, the WO_3 content increased from 26.67% to 61.13% after applying the algorithm. Based on the processing capacity of a medium-sized tungsten mine (60 T/h), approximately 120 kg of tungsten metal can be recovered daily, increasing annual economic benefits by over 5 million yuan.

Despite the excellent performance of the proposed algorithm in tungsten ore segmentation, it has two limitations:

(1) The current study only focuses on tungsten ores. For minerals with lower density (e.g., copper ores, density: 8.96 g/cm^3), the grayscale contrast of their X-ray images is relatively low, which may reduce the accuracy of concave point identification. In the future, it will be necessary to combine the energy spectrum differences in dual-energy X-rays to optimize the dynamic adjustment strategy of the grayscale standard deviation threshold.

(2) For ultra-complex adhesion with >8 particles (accounting for <5%, Table 1), the number of matching iterations of the algorithm needs to be increased to more than 50, prolonging the processing time to 8 ms. Although this still meets industrial real-time requirements (<10 ms), there is room for efficiency optimization. In subsequent work, a deep learning-based feature prediction module can be introduced to pre-locate the core adhesion region and reduce the search range.

Future research can be further extended to multi-mineral mixed sorting scenarios (e.g., tungsten-tin symbiotic ores). Combined with the global mineral supply chain security issue mentioned in the economic literature recommended by the reviewer, the application of the algorithm in low-grade mineral sorting can be explored to improve resource utilization efficiency and address long-term global mineral resource supply-demand challenges.

Author Contributions: Conceptualization, R.C. and S.Z.; methodology, R.C.; software, J.C.; validation, Y.Z.; formal analysis, R.C.; investigation, J.C.; resources, R.C.; data curation, J.C.; writing—review and editing, R.C. and Y.H.; visualization, Y.Z.; supervision, R.C.; project administration, J.C.; All authors have read and agreed to the published version of the manuscript.

Funding: This research was funded by National Natural Science Foundation of China (No. 12365026), Key Research and Development Project of Jiangxi Province (No. 20232BBE50013), Jiangxi Provincial Natural Science Foundation (No. 20242BAB25046).

Institutional Review Board Statement: Not applicable.

Informed Consent Statement: Not applicable.

Data Availability Statement: The original contributions presented in this study are included in the article. Further inquiries can be directed to the corresponding author.

Conflicts of Interest: The authors declare no conflicts of interest.

References

1. Jung, D.; Choi, Y. Systematic review of machine learning applications in mining: Exploration, exploitation, and reclamation. *Minerals* **2021**, *11*, 148. [CrossRef]
2. McCoy, J.T.; Auret, L. Machine learning applications in minerals processing: A review. *Miner. Eng.* **2019**, *132*, 95–109. [CrossRef]
3. Robben, C.; Wotruba, H. Sensor-based ore sorting technology in mining—Past, present and future. *Minerals* **2019**, *9*, 523. [CrossRef]
4. Wang, W.; Li, Q.; Zhang, D.; Fu, J. Image segmentation of adhesive ores based on MSBA-Unet and convex-hull defect detection. *Eng. Appl. Artif. Intell.* **2023**, *123*, 106185. [CrossRef]
5. Liu, Y.; Wang, X.; Zhang, Z.; Deng, F. Deep learning in image segmentation for mineral production: A review. *Comput. Geosci.* **2023**, *180*, 105455. [CrossRef]
6. Sun, G.; Huang, D.; Peng, Y.; Cheng, L.; Wu, B.; Zhang, Y. Efficient segmentation with texture in ore images based on box-supervised approach. *Eng. Appl. Artif. Intell.* **2024**, *128*, 107490. [CrossRef]
7. Liu, X.; Zhang, Y. Ore image segmentation method of conveyor belt based on U-Net and Res_UNet models. *J. Northeast. Univ. (Nat. Sci.)* **2019**, *40*, 1623.
8. Hu, X. Recent progress in experimental investigation of neutron irradiation response of tungsten. *J. Nucl. Mater.* **2022**, *568*, 153856. [CrossRef]
9. Omer, M.; Shizuma, T.; Hajima, R.; Koizumi, M. Nondestructive determination of isotopic abundance using multi-energy nuclear resonance fluorescence driven by laser Compton scattering source. *J. Appl. Phys.* **2024**, *135*, 184903. [CrossRef]
10. Li, Y.; Duan, Y. A method of ore image segmentation based on deep learning. In Proceedings of the Intelligent Computing Methodologies: 14th International Conference, ICIC 2018, Wuhan, China, 15–18 August 2018; Proceedings, Part III 14. Springer International Publishing: Berlin/Heidelberg, Germany, 2018.
11. Li, H.; Pan, C.; Chen, Z.; Wulamu, A. Ore image segmentation method based on u-net and watershed. Computers. *Mater. Contin.* **2020**, *65*, 563–578.
12. Mukherjee, D.P.; Potapovich, Y.; Levner, I.; Zhang, H. Ore image segmentation by learning image and shape features. *Pattern Recognit. Lett.* **2009**, *30*, 615–622. [CrossRef]

13. Li, F.; Liu, X.; Yin, Y.; Li, Z. DDR-Unet: A High Accuracy and Efficient Ore Image Segmentation Method. *IEEE Trans. Instrum. Meas.* **2023**, *72*, 5027920. [CrossRef]
14. Tan, S.; Ma, X.; Mai, Z.; Qi, L.; Wang, Y. Segmentation and counting algorithm for touching hybrid rice grains. *Comput. Electron. Agric.* **2019**, *162*, 493–504. [CrossRef]
15. Lin, P.; Chen, Y.M.; He, Y.; Hu, G.W. A novel matching algorithm for splitting touching rice kernels based on contour curvature analysis. *Comput. Electron. Agric.* **2014**, *109*, 124–133. [CrossRef]
16. Liao, M.; Zhao, Y.; Li, X.; Dai, P.; Xu, X.; Zhang, J.; Zou, B. Automatic segmentation for cell images based on bottleneck detection and ellipse fitting. *Neurocomputing* **2016**, *173*, 615–622. [CrossRef]
17. Zhang, W.; Li, H. Automated segmentation of overlapped nuclei using concave point detection and segment grouping. *Pattern Recognit.* **2017**, *71*, 349–360. [CrossRef]
18. Yao, Y.; Wu, W.; Yang, T.; Liu, T.; Chen, W.; Chen, C.; Li, R.; Zhou, T.; Sun, C.; Zhou, Y.; et al. Head rice rate measurement based on concave point matching. *Sci. Rep.* **2017**, *7*, 41353. [CrossRef] [PubMed]
19. Wang, L.; Hu, H.; Li, Z.; Dai, W. Splitting ore from X-ray image based on improved robust concave-point algorithm. *PeerJ Comput. Sci.* **2023**, *9*, e1263. [CrossRef]
20. He, L.; Wang, S.; Guo, Y. Detection of Pits by Conjugate Lines: An Algorithm for Segmentation of Overlapping and Adhesion Targets in DE-XRT Sorting Images of Coal and Gangue. *Appl. Sci.* **2022**, *12*, 9850. [CrossRef]
21. Sun, A.; Jia, W.B.; Hei, D.Q.; Yang, Y.; Cheng, C.; Li, J.T.; Wang, Z.L.; Tang, Y. Application of concave point matching algorithm in segmenting overlapping coal particles in X-ray images. *Miner. Eng.* **2021**, *171*, 107096. [CrossRef]
22. Ramer, U. An iterative procedure for the polygonal approximation of plane curves. *Comput. Graph. Image Process.* **1972**, *1*, 244–256. [CrossRef]
23. Suzuki, S. Topological structural analysis of digitized binary images by border following. *Comput. Vis. Graph. Image Process.* **1985**, *30*, 32–46. [CrossRef]
24. Bresenham, J.E. Algorithm for computer control of a digital plotter. *Semin. Graph. Pioneer. Efforts That Shaped Field* **1998**, *1*, 1–6.

Disclaimer/Publisher's Note: The statements, opinions and data contained in all publications are solely those of the individual author(s) and contributor(s) and not of MDPI and/or the editor(s). MDPI and/or the editor(s) disclaim responsibility for any injury to people or property resulting from any ideas, methods, instructions or products referred to in the content.